Check for updates

Small

NANO · MICRO small
www.small-journal.com

RESEARCH ARTICLE OPEN ACCESS

Titanium Oxide Thin Films With Metal Nanodisks as Plasmonic Metamaterial Photocatalyst Sheets for IPA-Assisted CO_2 Reduction

Benny Ku[1,2] | Lukas Feierabend[3] | Chun-Wei Su[1,2] | Chih-Chi Huang[1,2] | Gonzalo Aguila Flores[1] | Ulrich Plachetka[1] | Max C. Lemme[1,2]

[1]AMO GmbH, Advanced Microelectronic Center Aachen (AMICA), Aachen, Germany | [2]Chair of Electronic Devices, RWTH Aachen University, Aachen, Germany | [3]The Hydrogen and Fuel Cell Center (ZBT GmbH), Duisburg, Germany

Correspondence: Max C. Lemme (max.lemme@eld.rwth-aachen.de)

Received: 3 April 2026 | **Revised:** 15 August 2026 | **Accepted:** 10 October 2026

Keywords: artificial photosynthesis | nanoimprint lithography | photocatalysis | plasmonics | semiconductor fabrication | solar fuels

ABSTRACT

Plasmonic metals are considered a promising approach for enhancing the reactivity of solar-driven photocatalysts when used as co-catalytic nanostructures. However, optimizing the energy conversion efficiency is challenging because it requires precise control of the light-matter interactions at the nanoscale. In this work, we present metamaterial photocatalyst sheets that combine titanium dioxide (TiO_2) thin films and plasmonic metal nanodisks arranged in periodic arrays. Silver (Ag), gold (Au), platinum (Pt), and palladium (Pd) were used as nanodisk metals. We tested our photocatalyst sheets for generating solar fuels hydrogen (H_2) and methane (CH_4) from carbon dioxide (CO_2) using steamed water (H_2O) mixed with isopropyl alcohol (IPA) as a sacrificial agent under broadband (UV–vis–NIR) light exposure. Our Pt/TiO_2 and Pd/TiO_2 photocatalysts achieved gas product rates of 4.37 µmol cm^{-2} h^{-1} for H_2 and 0.42 µmol cm^{-2} h^{-1} for CH_4. The fabrication process flow is based on standard semiconductor fabrication methods, showing its potential for large-scale applications.

1 | Introduction

Addressing the impacts of global climate change requires a fundamental shift toward sustainable energy production [1–3]. One promising approach to mitigate global warming is to advance solar light-driven photocatalysis to decompose greenhouse gases and generate artificial fuels, also known as solar fuels [4]. The underlying (photo-)catalytic processes are water splitting [5, 6] and carbon dioxide (CO_2) reduction [7, 8]. These reactions generate solar fuels, such as hydrogen (H_2), methane (CH_4), carbon monoxide (CO), or methanol. A major advantage of solar fuels is their potential for decentralized generation within existing infrastructure [4] for applications in production, transportation, and energy generation. In addition, photocatalysis may contribute to a more sustainable chemical industry by reducing reliance on fossil fuels.

Significant efforts have been made in recent decades to develop efficient, stable, and scalable photocatalysts for solar fuel generation [9–11]. Various concepts and designs have been explored, including nanostructures, material heterostructures, metal-organic frameworks (MOFs) [12–14], plasmonic materials [15–17], perovskites [18–20], 2D materials [21–23], and their combinations [24]. While many of these approaches have led to improvements in photocatalytic reactivity and new scientific insights, a breakthrough that enables large-scale adoption has not yet been achieved because high-yield methods and sufficiently stable photocatalysts remain lacking [25].

This is an open access article under the terms of the Creative Commons Attribution License, which permits use, distribution and reproduction in any medium, provided the original work is properly cited.
© 2026 The Author(s). *Small* published by Wiley-VCH GmbH

One promising approach is the use of modular photocatalyst sheets, which can be mounted at large scale and provide both effectiveness and durability [26]. These sheets consist of photocatalyst materials deposited or grown on planar substrates via techniques such as spray coating [27], printing [28], or sputtering [29]. The performance of photocatalyst sheets has been further enhanced by integrating metamaterials, periodic nanostructures that enhance reaction efficiency through light trapping, plasmonic coupling, and precise control over individual reaction centers [30–32]. The potential of metamaterials has been demonstrated in photocatalytic applications such as water splitting [33, 34], water purification [35], and CO_2 reduction [36].

A frequently used photocatalyst material is the semiconductor titanium dioxide (TiO_2) because of its low cost, high availability, and photostability [9, 10, 37]. In the anatase crystal phase, TiO_2 has a large bandgap of 3.25 eV, restricting its photoexcitation and photocatalytic activity to the ultraviolet (UV) range below 387 nm. Plasmonic metal nanostructures in contact with TiO_2 can drive collective dipole oscillations and extend the photocatalytic activity to the visible wavelength range [38, 39]. The metal–TiO_2 contact results in the formation of a Schottky or Ohmic barrier that can be crossed only by hot electrons, i.e., highly energetic electrons resulting from plasmonic interactions [40]. These charge-carriers can reach the surface of the structure, where they contribute to chemical reactions.

Here, we present metamaterial photocatalyst sheets based on plasmonic nanodisk arrays on titanium dioxide (TiO_2) thin films for photocatalytic IPA-assisted CO_2 reduction. We investigated silver (Ag) [41–43], gold (Au) [44–47], platinum (Pt) [48–52], and palladium (Pd) [53–55] as plasmonic metals. Ag and Au were chosen because of their strong plasmonic properties [56], whereas Pt and Pd were selected for their remarkable adsorption properties for photocatalytic reactions [57, 58]. We characterized the geometrical, crystalline, and optical properties of our photocatalysts via scanning electron microscopy (SEM), atomic force microscopy (AFM), ultraviolet-visible-near infrared (UV–vis–NIR) photospectroscopy, and Raman spectroscopy. The photocatalytic performance of the photocatalyst sheets was assessed in a custom-built chamber reactor for solar fuel generation of H_2 and CH_4 through IPA-assisted water splitting and CO_2 reduction. We conducted finite-differences time-domain (FDTD) simulations to elucidate their internal light-matter interactions. Finally, we propose a schematic band diagram and a corresponding mechanism for the charge-carrier dynamics in our photocatalytic metamaterial.

2 | Results and Discussion

2.1 | Photocatalyst Design

The photocatalyst sheets were fabricated via standard semiconductor fabrication techniques, with nanoimprint lithography (NIL) as the key processing step [33–35, 59, 60]. This method provides a deterministic, reproducible arrangement of periodic metal nanostructures while enabling large-scale manufacturing [61, 62]. We used Ag, Au, Pt, and Pd metals as plasmonic nanostructures on the TiO_2 thin film, labeled "Ag/TiO_2", "Au/TiO_2", "Pt/TiO_2", and "Pd/TiO_2", respectively. Details of the fabrication process are described in the Methods section and illustrated in Figure S1.

Our metamaterial structures are based on periodic nanodisk arrays that are patterned on a TiO_2 thin film. The geometrical parameters are shown in a schematic cross-section in Figure 1a, and characterized by period P, nanodisk diameter D, nanodisk height H_{ND}, and the TiO_2 thin-film thickness H_{SC}. In this work, we selected P = 300 nm, D = 150 nm, H_{ND} = 30 nm, and H_{SC} = 250 nm. These values were defined by inherent specifications of the fabrication process; particularly the period P is based on our laser interference lithography setup (see Methods section). The nanodisk height H_{ND} = 30 nm is set primarily by lift-off process limitations in the fabrication flow.

Simulations of the scattering, absorption, and extinction spectra for Ag/TiO_2, Au/TiO_2, Pt/TiO_2, and Pd/TiO_2 confirmed plasmonic activity for these parameters (see simulations and Figures S2–S5). The photocatalytic processes occurring on the metamaterial are illustrated in Figure 1b: CO_2 and H_2O molecules adhere on the surface, where CO_2 is reduced, and water is split. Figure 1c shows the proposed band diagram schematic for our metamaterial structures. We assumed the valence band (VB) and conduction band (CB) edges of anatase TiO_2 to be −7.25 and −4.05 eV, respectively [63]. Moreover, we treated anatase TiO_2 as an n-type semiconductor with a bandgap of E_G = 3.25 eV, an electron affinity of 5.1 eV, and a work function of 4.45 eV [64, 65]. The work functions of the plasmonic metals typically range from 4.26 to 4.74 eV, 5.1–5.47 eV, 5.22–5.60 eV, and 5.12–5.93 eV, for Ag, Au, Pt, and Pd, respectively [66]. Once the metal and the TiO_2 layer are in contact, their Fermi levels E_F align, causing a shift in the VB and CB levels. In the case of Ag, an Ohmic junction forms with TiO_2 because of its lower work function (dashed line at the metal/TiO_2 interface). Au, Pt, and Pd form Schottky junctions when in contact with TiO_2, as their work function is larger than the electron affinity of TiO_2 (Figure 1c, solid line at the metal/TiO_2 interface). Upon illumination with broadband light, the UV component of the light is absorbed in the TiO_2 layer, creating electron–hole pairs. If these carriers do not recombine, they can participate in reduction and oxidation (redox) reactions at the photocatalyst surface and trigger the reaction processes for water splitting and CO_2 reduction.

Additionally, electrons in the metallic nanodisks can be excited into collective oscillations upon light exposure, known as localized surface plasmon resonances (LSPR, see simulations below). These electrons can reach a high-energy state (LSPR state), i.e., they become hot electrons with sufficient energy to overcome the Schottky barrier and enter the conduction band of the TiO_2 semiconductor (in the case of Au, Pt, and Pd). The absence of electrons in the metal can also generate high-energy holes, known as hot holes [67], which can contribute to oxidation reactions from the metal nanodisk surface.

Since the Ag/TiO_2 interface forms an Ohmic contact (dashed line at the metal/TiO_2 interface), electrons in the metal layer can also be excited to the LSPR state and more easily migrate into the TiO_2 layer, where they contribute to the reduction reactions [68]. Notably, Ag can form a native oxide that weakens its plasmonic properties [69]. However, silver oxide (Ag_2O) is also a known photocatalyst [70], which may offset the contradictory

16136829, 0, Downloaded from https://onlinelibrary.wiley.com/doi/10.1002/smll.76358 by Universitatsbibliothek RWTH Aachen University, Wiley Online Library on [03/11/2026]. See the Terms and Conditions (https://onlinelibrary.wiley.com/terms-and-conditions) on Wiley Online Library for rules of use; OA articles are governed by the applicable Creative Commons License

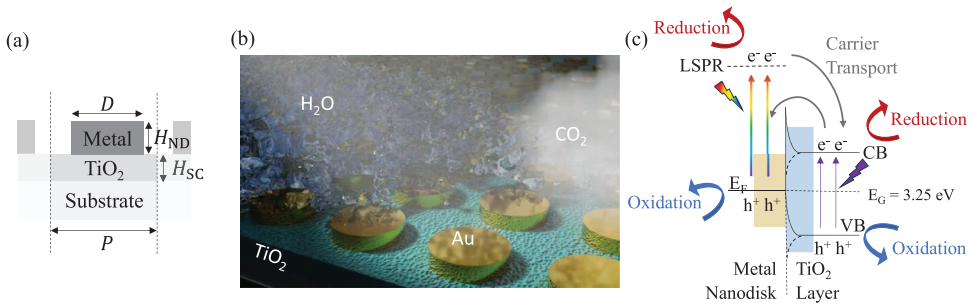


FIGURE 1 | (a) Schematic cross-section of the plasmonic nanodisk metamaterial photocatalyst sheet design. The geometrical parameters are the nanodisk diameter D, nanodisk height H_{ND}, semiconductor thickness/height H_{SC}, and period P. (b) Conceptual visualization of the metamaterial photocatalyst sheet surface with adhering H_2O and CO_2 molecules, representing the water splitting and CO_2 reduction process. (c) Proposed bandgap diagram schematic of the nanodisk metamaterial photocatalyst sheet. The solid line at the metal/TiO_2 interface indicates a Schottky junction, whereas the dashed line indicates an Ohmic junction. In the metamaterial structure, charge-carriers in the metal are excited by visible light exposure into the LSPR state. At the same time, they can also be photoexcited in the TiO_2 layer by UV-light exposure. Both types of excited charge-carriers can then participate in redox reactions.

effects of oxidation on the photocatalytic process in Ag/TiO_2 metamaterials.

We emphasize that our proposed pathway is a model inferred from product kinetics and junction energetics rather than a directly observed mechanism. Its direct validation would require further identification of surface-bound intermediates, for example by in situ infrared spectroscopy in a reflectance- or transmission-based configuration compatible with our photocatalyst sheets [71, 72].

2.2 | FDTD Simulations

We conducted finite-difference time-domain (FDTD) simulations with Ansys Lumerical to compute the electric fields (E-field) arising from photon/plasmon interactions to elucidate the light-matter interactions of the metamaterial structures. This numerical Maxwell equation solver accounts for scattering, absorption, extinction, and E-field enhancements of a normalized incident light source, making it suitable for simulating surface plasmon resonances (SPR) of arbitrary geometry. In the computations, the geometric parameters of the nanodisks were centered around our experimental values of $H_{ND} = 30$ nm, D = 150 nm, and P = 300 nm in the XY plane. Surface roughness was not considered in the simulation. The simulated TiO_2 layer was set to $H_{SC} = 250$ nm on top of a SiO_2 substrate. Further details of the FDTD simulations are provided in the Methods section.

The simulated E-field enhancements of the Ag/TiO_2, Au/TiO_2, Pt/TiO_2, and Pd/TiO_2 photocatalyst sheets are plotted as a function of λ in the range of 300–1000 nm (UV–vis–NIR) in Figure 2. The different light responses are attributed to differences in the dielectric constants of the metals. The real part of the complex permittivity of a material, ε_1, determines its polarization response, and the imaginary part, ε_2, determines its optical loss [73]. Their ratio $|\varepsilon_1/\varepsilon_2|$ is an indicator of their LSPR response. The ratios for Ag, Au, Pt, and Pd are 37.96, 7.33, 0.71, and 0.91, respectively [56]. Based on these numbers, Ag is expected to exhibit the highest LSPR response, followed by Au. However, the native oxidation of Ag can significantly lower its LSPR response [69]. The ratios of Pt and Pd yield small LSPR responses. The simulations show that all nanodisk structures confine incident light and act as plasmonic resonators due to their subwavelength geometries. All four metals exhibit similar E-field enhancements at the outer boundaries of the nanodisks. These are regions with high densities of hot electrons. The Ag/TiO_2 and Au/TiO_2 E-field enhancements are on the order of 100 in the Vis–NIR range (600–1000 nm). The Ag/TiO_2 also shows strong plasmonic activity at 400 nm. The LSPRs are less prominent for Pt/TiO_2 and Pd/TiO_2 in the UV–vis range, indicating that they are plasmonic absorbers rather than resonators. Pd/TiO_2 shows the most intense LSPR in the NIR range, with an E-field enhancement of approximately 100, whereas Pt/TiO_2 has the lowest value ranging between 50 and 100.

We also explored the influence of the period P on the scattering, absorption, and extinction of each photocatalyst design, though the fabrication process dictated the experimental P (see Figures S2–S5). All data show a plateau at 60%–70% absorption and extinction for wavelengths of $\lambda < 400$ nm. Here, the behavior is independent of P, because the TiO_2 layer absorbs the light once its energy reaches the bandgap of 3.25 eV (i.e., its absorption edge at $\lambda = 387$ nm) [74]. Ag/TiO_2 (Figure S2) and Au/TiO_2 (Figure S3) show high scattering activities that vary with P, exceeding 80%. These simulations also confirm that P = 300 nm is a good choice, as a lower P would lead to lower scattering activity, i.e., weaker plasmonic properties. In contrast, Pt/TiO_2 (Figure S4) and Pd/TiO_2 (Figure S5) show scattering activity in the 10%–20% range at P = 300 nm. Here, our simulations suggest that P = 200 nm would yield better plasmonic properties, although it is not attainable with our proposed cost-effective NIL-based fabrication scheme.

The FDTD simulations provide reliable information on E-field distributions and charge-carrier densities. However, they are limited in their ability to predict photocatalytic activity, because this complex process is influenced by factors such as the electronic structure of the photocatalyst, thermodynamics, energy levels of reactants and products, and charge-carrier dynamics. These effects can only be captured (to a degree) by multiphysics modeling, which is beyond the scope of this work [75].

16136829, 0, Downloaded from https://onlinelibrary.wiley.com/doi/10.1002/smll.76358 by Universitatsbibliothek RWTH Aachen University, Wiley Online Library on [03/11/2026]. See the Terms and Conditions (https://onlinelibrary.wiley.com/terms-and-conditions) on Wiley Online Library for rules of use; OA articles are governed by the applicable Creative Commons License

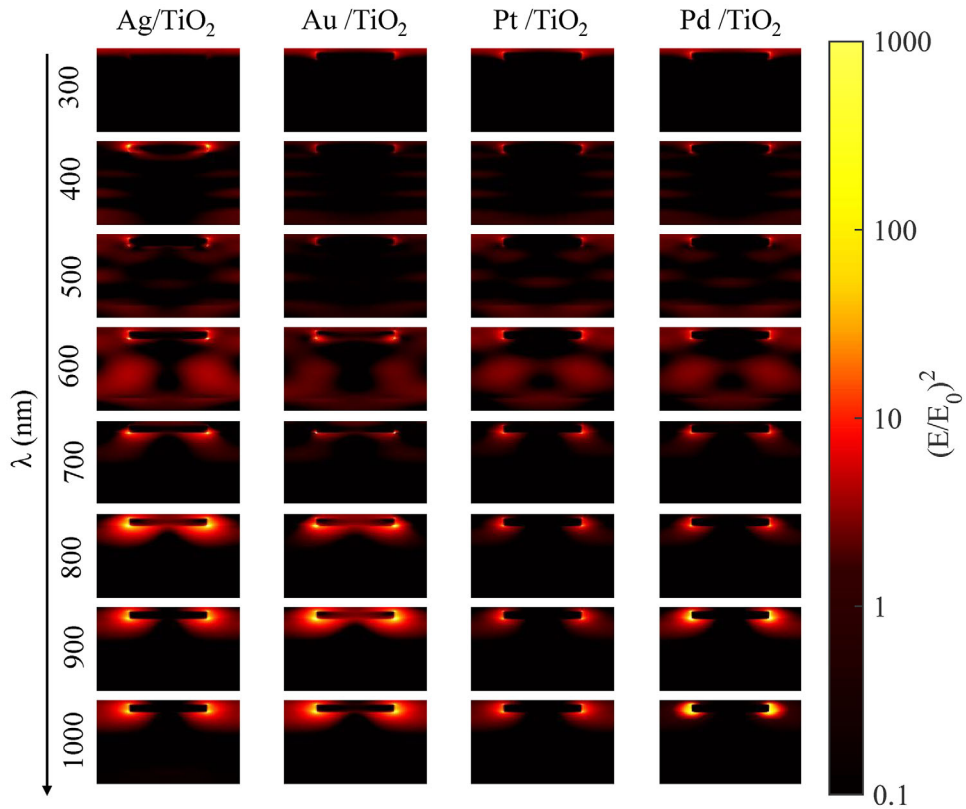


FIGURE 2 | Cross-sectional FDTD simulation results of the E-field enhancement of Ag/TiO_2, Au/TiO_2, Pt/TiO_2, and Pd/TiO_2 metamaterial structures. The plasmonic nanodisks have $H_{ND} = 30$ nm, D =150 nm, and $P = 300$ nm. The nanodisks are placed on a TiO_2 layer with $H_{SC} = 250$ nm. For comparison, the E-field enhancement is plotted on a fixed logarithmic scale from 0.1 to 1000. The results are plotted as a function of the incident wavelength from 300 to 1000 nm to cover the UV–vis–NIR range.

2.3 | Characterization

The photocatalysts were analyzed by SEM and AFM to evaluate their structural morphology and geometric parameters. A top-view and a cross-sectional SEM image of the Au/TiO_2 photocatalyst are shown in Figure 3a,b, respectively. In addition to the information on period and morphology, Figure 3b further reveals the crystal grain structure of the TiO_2 layer. The image indicates the presence of a crystalline phase formed during annealing (Figure S6) [74, 76]. This is the anatase phase, which is favorable for photocatalytic processes as it increases the surface area and improves charge-carrier separation at the grain boundaries compared to the amorphous phase [77]. The height profiles of the metasurfaces were measured by AFM (details in Methods section). The example in Figure 3c shows an array of Au nanodisks on TiO_2 with $H_{ND} = (33 \pm 3)$ nm and $D = (153 \pm 3)$ nm, consistent with our design. The pattern covers the entire sample's surface area of (5×5) cm^2.

Raman spectra of the TiO_2 films confirmed the anatase phase with characteristic peaks at 141, 193, 513, and 635 cm^{-1} (Figure 3d). The additional peak at 392 cm^{-1} indicates the presence of the brookite phase, possibly originating from the annealing process at 650°C. This high-temperature process step is required because it optimizes the catalytic properties of the anatase phase. Although the brookite phase also starts to form [74, 76] it is not critical for the photocatalytic performance [78]. Pt/TiO_2 and Pd/TiO_2 are less plasmonically active and show lower Raman intensities, as predicted in our simulations. We nevertheless included Pt and Pd in the experiments because of their strong intrinsic catalytic activity in water splitting and CO_2 reduction [58]. The characteristic anatase and brookite peaks are present in both the bare TiO_2 reference and the nanodisk-patterned samples, indicating that the nanodisk fabrication process preserves the anatase phase of the underlying oxide film.

We further measured the absorption spectra of all photocatalyst sheets with a UV–Vis–NIR photospectrometer (Figure 3e). The spectrum of the bare TiO_2 thin film (black dashed line) differs significantly from the spectra of plasmonic metal nanodisks (colored lines), especially in the visible wavelength range. The nanodisk arrays exhibit multiple absorption peaks and dips arising from their periodicity and subwavelength nanostructures, which give rise to diffractive optical effects and interference. Moreover, Wood–Rayleigh anomalies lead to varying energies across the diffraction orders of the incident light [79, 80]. These effects manifest for wavelengths below 650 nm, with slight variations in the peak and dip positions because of different refractive indices of the metals and minor variations in their fabricated geometries. The broader peaks beyond 650 nm are the LSPR peaks for Ag/TiO_2 and Au/TiO_2, located at 786 nm and 892 nm, respectively, whereas the peaks for Pt/TiO_2 and Pd/TiO_2 are in the NIR range.

16136829, 0, Downloaded from https://onlinelibrary.wiley.com/doi/10.1002/smll.76358 by Universitatsbibliothek RWTH Aachen University, Wiley Online Library on [03/11/2026]. See the Terms and Conditions (https://onlinelibrary.wiley.com/terms-and-conditions) on Wiley Online Library for rules of use; OA articles are governed by the applicable Creative Commons License

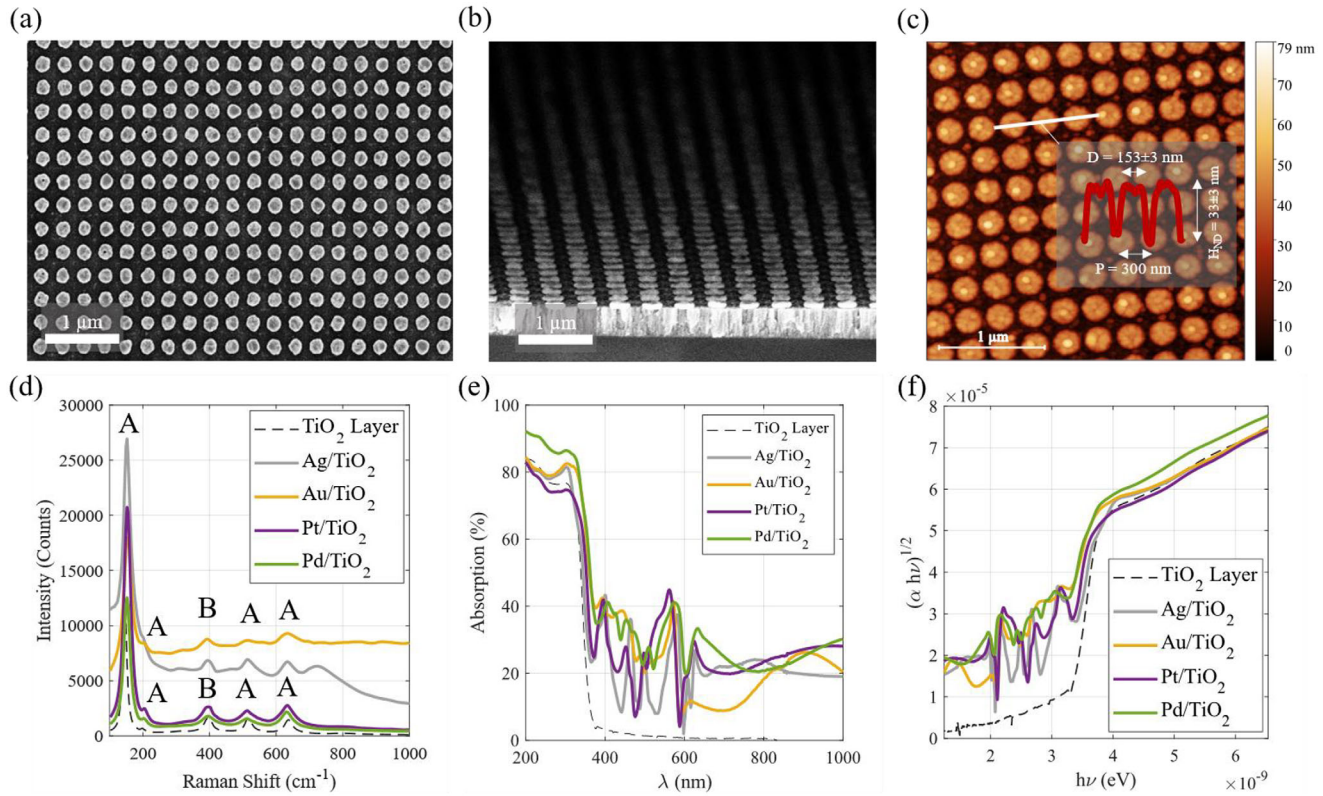


FIGURE 3 | Photocatalyst characterization of the TiO_2 thin film patterned with plasmonic metal nanodisks. (a) Top-down and (b) cross-sectional SEM image of Au/TiO_2 (scale bar: 1 µm). (c) AFM topography image of Au/TiO_2. (d) Raman spectra of a reference sample with a bare TiO_2 layer (black dashed line) and the Ag/TiO_2 (gray), Au/TiO_2 (yellow), Pt/TiO_2 (purple), and Pd/TiO_2 (green) metamaterials. The spectra show the characteristic peaks of the anatase TiO_2 phase (A) (and brookite phase (B), see discussion in the main text) and an overall enhanced signal depending on the different metals. (e) Absorption spectra from UV–Vis–NIR measurement for the same set of samples, showing the absorption activity in the visible–NIR range created by the different metals. (f) Tauc plot analyses of the absorption spectra, indicating a bandgap of 3.25 eV for the TiO_2 layer, 3.09 eV for Ag/TiO_2, 2.62 eV for Au/TiO_2, 2.93 eV for Pt/TiO_2, and 2.81 eV for Pd/TiO_2 (see also Figure S7).

We conducted Tauc analyses to estimate the effective bandgap of each metamaterial (Figure 3f). The extracted bandgap of the TiO_2 thin film was 3.25 eV, which is in agreement with the literature data (Figure S7a) [74]. The plasmonic nanodisks on the TiO_2 thin film led to a redshift of the absorption edges, which resulted in an effective bandgap narrowing of the entire metamaterial stack. The detailed Tauc plots are shown in Figure S7b–e, revealing effective bandgaps of 3.09, 2.62, 2.93, and 2.81 eV for Ag/TiO_2, Au/TiO_2, Pt/TiO_2, and Pd/TiO_2, respectively.

2.4 | Photocatalytic Measurements

The photocatalyst sheets were tested in a custom-made lab-scale photocatalytic flow reactor that operates entirely in the gas phase. A photograph and a schematic cross-sectional image are shown in Figure 4a,b. We conducted the measurements at a CO_2 gas flow rate of 1 sccm and a 0.6 ml h^{-1} liquid feed flow of a mixture of deionized water and 1 mol L^{-1} IPA, which was used as a hole scavenger to enhance the measurement signals [81]. The metallic reactor frame was heated to a constant temperature of 120°C to maintain a gas phase in the reaction chamber. The liquid feed flow was mixed with CO_2 upstream of the reaction chamber within an embedded piece of microporous carbon felt (Figure 4b) to control evaporation, forming the combined CO_2/IPA/H_2O gas-phase feedstock used in our main experiments. Mass flow controllers regulated the flow rates of the incoming reactant gases, and the outgoing product gases were analyzed in real time by a mass spectrometer (MS). Before entering the MS capillary, the condensed liquid was separated from the product stream. The (5 × 5) cm^2-sized photocatalyst was irradiated by a 150 W metal-halide lamp (Figure S8) at a distance of 20 cm from the photocatalytic surface, separated by a fused silica glass window with a thickness of 3 mm, resulting in an overall flux density of approximately 500 mW cm^{-2}. The expected catalytic reactions are listed in Table 1, describing the generation of protons (H^+), H_2, and CH_4 in Equations S1–S3, respectively.

The H_2 (blue squares) and CH_4 (orange squares) yields for the different photocatalyst sheets are plotted in Figure 5a,b for Ag/TiO_2 (gray line), Au/TiO_2 (yellow line), Pt/TiO_2 (green line), and Pd/TiO_2 (purple line). They were obtained from the MS signals, which were calibrated with a known test gas to determine the quantities of each substance (Figure S9). Afterward, they were processed using Equation S10 to convert volume concentration data to the amount of substance (Figures S10 and S11). The data show that the H_2 and CH_4 yields for each photocatalyst sheet depend on reaction time, reaction rate, and catalytic selectivity of the different metal nanodisks. The measurements were stopped once the gas evolution saturated in the MS raw data on a

16136829, 0, Downloaded from https://onlinelibrary.wiley.com/doi/10.1002/smll.76358 by Universitatsbibliothek RWTH Aachen University, Wiley Online Library on [03/11/2026]. See the Terms and Conditions (https://onlinelibrary.wiley.com/terms-and-conditions) on Wiley Online Library for rules of use; OA articles are governed by the applicable Creative Commons License

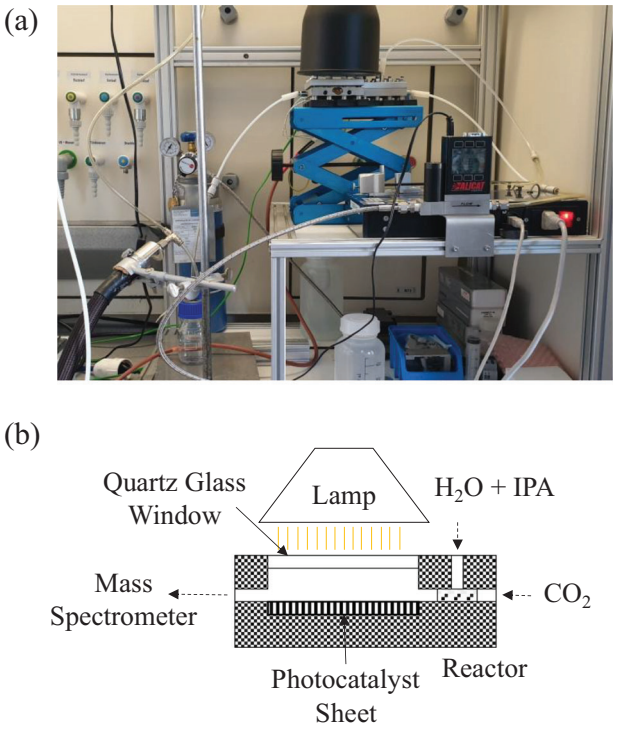


FIGURE 4 | (a) Photograph and (b) schematic cross-sectional illustration of the lab-scale photocatalytic reactor. The gaseous feedstock (IPA-mixed H_2O and CO_2) flows into the reactor chamber and reacts on the photocatalyst sheet surface, while a light source illuminates it. A mass spectrometer then analyzes the output gas.

TABLE 1 | Overview of the relevant reaction equations in this work for water splitting. CO_2 reduction, and IPA degradation [95, 96].

Process	Reaction equation	Nos.
Water splitting	$2\,H_2O + 4\,h^+ \longrightarrow O_2 + 4\,H^+$	(1)
	$2\,H^+ + 2\,e^- \longrightarrow H_2$	(2)
CO_2 reduction	$CO_2 + 8\,H^+ + 8\,e^- \longrightarrow CH_4 + 2\,H_2O$	(3)
IPA degradation	$(CH_3)_2CHOH + 2h^+ \longrightarrow (CH_3)_2CO + 2H^+$	(4)

logarithmic scale (Figures S12–S15). This effect was observed after different measurement times for each sample, e.g., at t = 5000 s for Ag/TiO_2 (Figure S12) and already at t = 4000 s for Au/TiO_2 (Figure S13).

In each measurement, the reactor was held at the operating temperature of 120°C in the dark, with the lamp running continuously at a stable power but the beam path to the reactor blocked, until the feedstock flow and chamber conditions reached a stable baseline. The beam path was then unblocked to begin illumination (marked as 'light on' in the MS raw data; Figures S12–S15). No H_2 or CH_4 evolution was observed during this dark phase; gas evolution began only after the beam path was unblocked, confirming that the reaction is light-driven and not the sole result of thermal or dark chemical processes at 120°C. We note, however, that we were unable to directly measure the local temperature at the nanodisk surface under illumination, so a minor localized photothermal contribution at the nanodisk edges cannot be fully excluded.

All measurements show linear H_2 and CH_4 yields with time before saturation. We observed a slight time delay in the CH_4 formation (orange curve) after H_2 generation (blue curve) started (Figures S12–S15). Depending on the metal, this delay ranged from 200 to 500 s, which suggests that CH_4 formation utilizes protons (H^+) generated from water splitting: H^+ that has not reacted to H_2 (Table 1, Equation S2) can then support the conversion of CO_2 into CH_4 (Table 1, Equation S3). Control experiments without a photocatalyst sheet (Figure S16) showed no detectable gas evolution under illumination, confirming that the reactor and $CO_2/IPA/H_2O$ feedstock do not react under light or heating alone. A bare TiO_2 thin film without metal nanodisks (Figure S17) produced only a small H_2 signal and no detectable CH_4 under the same broadband illumination, substantially lower than any of the metal nanodisk samples. This confirms that the metal nanodisks are responsible for the large majority of the observed photocatalytic activity, while UV excitation of TiO_2 alone contributes only a minor fraction.

Furthermore, we conducted control measurements without CO_2 in the feedstock (Figures S20–S23). Instead of the $CO_2/IPA/H_2O$ feedstock in the main experiment, an $N_2/IPA/H_2O$ feedstock was used. Under these CO_2-free conditions, the CH_4 signal remained detectable, reduced by a metal-dependent factor of approximately 5.6 for Pt/TiO_2 and 1.8 for Ag/TiO_2. This indicates that the contribution of the IPA sacrificial agent as a secondary carbon source varies with the metal: for Pt/TiO_2, CO_2 reduction is the dominant source of the CH_4, whereas for Ag/TiO_2, a substantial fraction of the CH_4 originates from IPA or its oxidation products rather than from CO_2 alone. A precise quantification of the CO_2-derived fraction would require $^{13}CO_2$ isotope-labeling experiments [82].

We further conducted control measurements without IPA in the feedstock (Figure S24), replacing the $CO_2/IPA/H_2O$ feedstock by CO_2/H_2O. Under IPA-free conditions, no significant H_2 or CH_4 evolution was observed for Au/TiO_2, Pt/TiO_2, and Pd/TiO_2. Only Ag/TiO_2 showed a small product signal marginally above the detection baseline. This confirms that IPA is required for measurable photocatalytic activity under our reaction conditions, acting as an efficient hole scavenger that suppresses electron–hole recombination [83].

Together with the CO_2-free control above, these measurements indicate that CO_2 reduction is the dominant source of the CH_4 observed under the full $CO_2/IPA/H_2O$ feedstock for Pt/TiO_2, while IPA both enables the reaction by scavenging photogenerated holes and contributes a fraction of the CH_4 as a secondary carbon source.

We observed the longest reaction times for our Ag/TiO_2 photocatalyst, whereas Au/TiO_2 showed moderate H_2 and CH_4 formation times. With Pt/TiO_2, the shortest H_2 formation times of approximately 1500 s occurred. In contrast, Pd/TiO_2 achieved the shortest CH_4, but the longest H_2 formation times, suggesting that CO_2 reduction with H^+ ions was preferred over H_2 formation with this catalyst. These results show differences in catalytic formation

16136829, 0, Downloaded from https://onlinelibrary.wiley.com/doi/10.1002/smll.76358 by Universitatsbibliothek RWTH Aachen University, Wiley Online Library on [03/11/2026]. See the Terms and Conditions (https://onlinelibrary.wiley.com/terms-and-conditions) on Wiley Online Library for rules of use; OA articles are governed by the applicable Creative Commons License

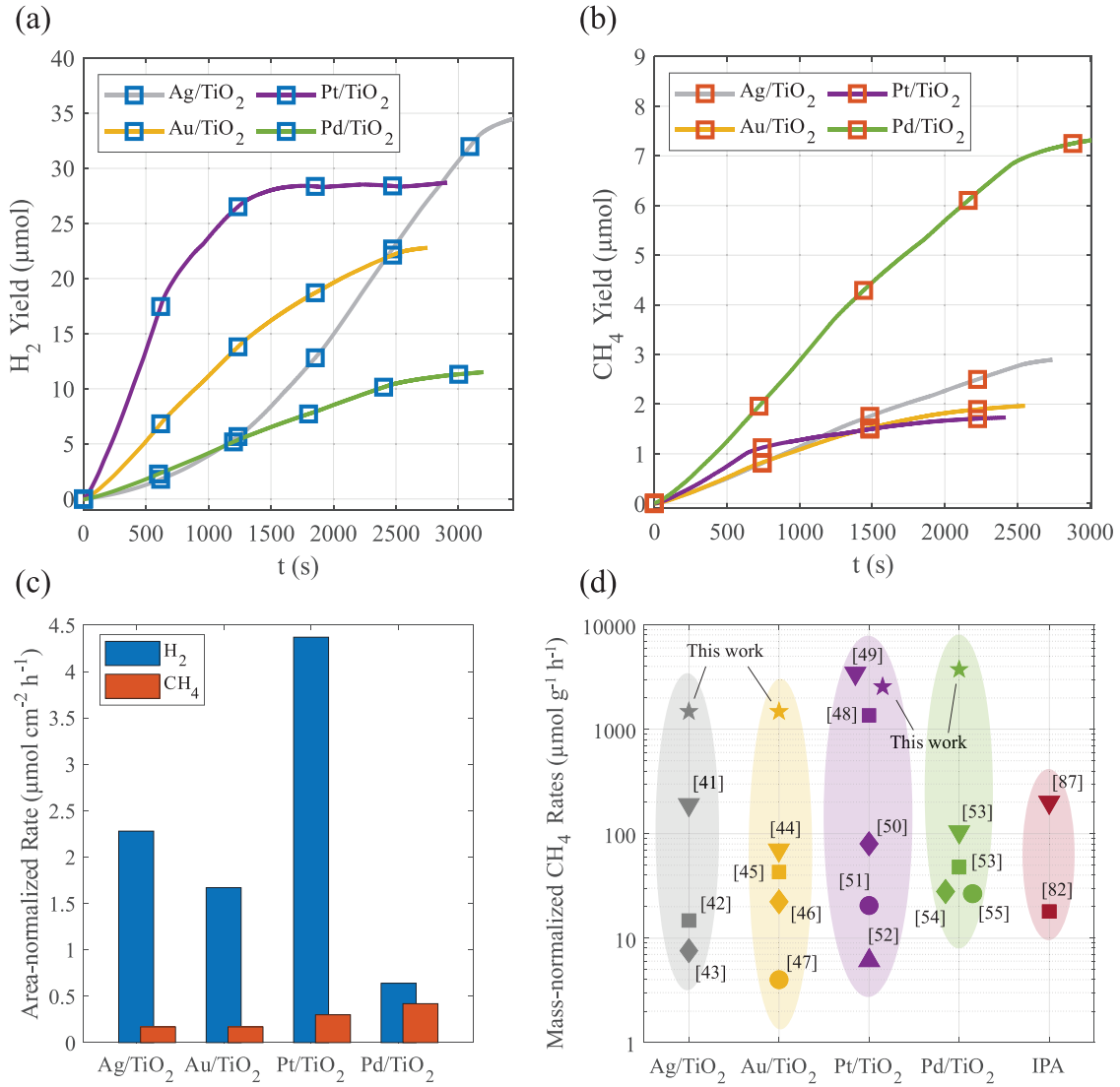


FIGURE 5 | (a) H_2 and (b) CH_4 generation measured by mass spectrometry for the Ag/TiO_2 (gray line), Au/TiO_2 (yellow line), Pt/TiO_2 (green line), and Pd/TiO_2 (purple line) metamaterial photocatalyst sheets. (c) H_2 and CH_4 gas generation rates normalized by the photocatalyst area of each photocatalyst sheet. (d) Benchmark plot of mass-normalized CH_4 production rates with those of plasmonic TiO_2-based photocatalysts and photocatalytic IPA conversion found in the literature.

selectivity among the samples, attributable to differences in charge-carrier dynamics and surface kinetics between the respective metals [84, 85]. Direct electrochemical characterization of the charge-carrier behavior, such as photocurrent or impedance measurements, is typically performed in a liquid electrolyte and is therefore not directly compatible with the gas-phase environment (CO_2/IPA/H_2O at 120°C) in which our photocatalysts operate.

The gas production rates normalized by time and photocatalyst area for H_2 and CH_4 are summarized as bar plots in Figure 5c for each photocatalyst. They were obtained from the raw data using a Bayesian noise filter [86] and linear regression (Figures S10 and S11). This data normalization is an important metric to practically express the efficiency of a photocatalyst sheet. Our photocatalyst sheets had a total area of 25 cm^2. Moreover, it is a common approach to also express the rate normalized by photocatalyst mass, as raw materials are essential cost factors. We derived their masses using geometric assumptions supported by SEM and AFM data. Our mass calculation accounts for the mass of the TiO_2 layer and the plasmonic nanodisk arrays (see Equation S5 for details). Accordingly, the photocatalyst mass ranges from 2.8 to 3.0 mg per 25 cm^2, depending on the choice of metal (Table S1). The lithographically defined geometry of the nanodisk arrays further allows the metal loading of each sample to be calculated directly from the geometry and the mass density of each metal, rather than determined by destructive elemental analysis (Table S1). Table 2 summarizes the absolute, area-normalized, and mass-normalized product rates.

We chose this mass-normalization approach to benchmark our work because data on area-normalized rates are scarce in the literature. The corresponding benchmark plot for the CH_4 production rate is shown in Figure 5d. H_2 production rates were not benchmarked because comparable data in the literature are often lacking, even though water splitting is often performed simultaneously in many publications on photocatalytic CO_2 reduction.

16136829, 0, Downloaded from https://onlinelibrary.wiley.com/doi/10.1002/smll.76358 by Universitatsbibliothek RWTH Aachen University, Wiley Online Library on [03/11/2026]. See the Terms and Conditions (https://onlinelibrary.wiley.com/terms-and-conditions) on Wiley Online Library for rules of use; OA articles are governed by the applicable Creative Commons License

TABLE 2 | Summary of the extracted absolute, area-normalized, and mass-normalized product rate of all photocatalyst sheets.

Photocatalyst	Absolute product rate [μmol h^{-1}]		Area-normalized product rate [μmol cm^{-2} h^{-1}]		Mass-normalized product rate [μmol g^{-1} h^{-1}]	
	H_2	CH_4	H_2	CH_4	H_2	CH_4
Ag/TiO_2	56.88	4.15	2.28	0.17	20 314	1484
Au/TiO_2	41.76	4.30	1.67	0.17	14 400	1482
Pt/TiO_2	109.13	7.42	4.37	0.30	37 631	2558
Pd/TiO_2	15.92	10.47	0.64	0.42	5687	3740

For our CH_4 plot, we selected comparable photocatalytic systems based on Ag-TiO_2 (gray), Au-TiO_2 (yellow), Pt-TiO_2 (green), and Pd-TiO_2 (purple). Note that we used the hyphen (-) in the nomenclature to indicate the general material system, as opposed to the forward slash (/) for the specific plasmonic nanodisk metamaterial photocatalyst sheets in our work. We also included literature data on photocatalytic IPA conversion (red) [82, 87]. The underlying data and more benchmarking details can be found in Table S2. Our normalized results for Ag/TiO_2, Au/TiO_2, and Pd/TiO_2 show significant improvement factors of 7.8, 21.1, and 35.9, respectively, over the state of the art. Our normalized Pt/TiO_2 data is close to the highest CH_4 production rate reported to date [48]. Overall, we attribute the high mass-normalized gas rates to the efficient thin-film structure used in our photocatalyst design.

One major drawback of our photocatalysts is their limited activity. All measurements showed decreasing gas rates over time that saturated within one hour (Figures S12–S15). The characterization by SEM (Figure 3a,b), AFM (Figure 3c), Raman spectroscopy (Figure 3d), and UV–vis (Figure 3e,f) were conducted after the photocatalytic measurements, showing that the metastructure remains ordered, the anatase TiO_2 peaks remain present, and the absorption peaks are retained. Therefore, these results indicate that there is no structural failure such as delamination of the metastructure, excluding it being the root-cause for its limited activity.

We attribute it most plausibly to a site-blocking effect of the active reaction area by strongly bound intermediates from water splitting [88] and CO_2 reduction [89]. Similar effects are apparent in several publications [88, 90, 91], but the origins are rarely discussed in detail. Distinguishing reversible surface site-blocking from irreversible deactivation over longer timescales would require dedicated cycling and regeneration tests, which lie beyond the scope of the present study.

Our experimental data show H_2 generation rates of Pt/TiO_2 > Ag/TiO_2 > Au/TiO_2 > Pd/TiO_2 (highest to lowest). In the case of the CH_4 generation rate, the order is Pd/TiO_2 > Pt/TiO_2 > Ag/TiO_2 > Au/TiO_2. These results contradict the expectation from the permittivity ratios $|\varepsilon 1/\varepsilon 2|$ (Section 2.2), which rank Ag and Au as the strongest plasmonic metals. However, our FDTD simulations show that the near-field enhancements are in fact similar across all four metals, so the optical response alone does not predict the activity ordering. We attribute the superior performance of Pt/TiO_2 and Pd/TiO_2 to the combination of optical light-harvesting with their more favorable junction energetics and their well-established adsorption properties towards H_2O, CO_2, and their intermediates [58, 92].

In addition, control experiments with Al and Cu nanodisks on TiO_2 were also conducted, as shown in Figures S18 and S19, respectively. However, they did not show any significant reactivity despite having plasmonic properties and forming Ohmic (Al/TiO_2) and Schottky (Cu/TiO_2) junctions [93]. This indicates that neither plasmonic response nor junction formation alone is sufficient for photocatalytic activity. Measurable performance instead requires the combination of plasmonic light harvesting in the visible range, favorable junction energetics for carrier extraction, and suitable surface chemistry, as shown by Ag/TiO_2, Au/TiO_2, Pt/TiO_2, and Pd/TiO_2.

We also examined the influence of the nanodisk height on the photocatalytic performance. Reference Pd/TiO_2 samples with increased nanodisk heights H_{ND} = 50 nm and H_{ND} = 70 nm, fabricated with a modified lift-off process, were tested under identical reaction conditions. Although FDTD simulations show that a larger metallic volume couples more strongly with the incident light (Figure S25), the photocatalytic measurements showed lower H_2 and CH_4 generation than for the standard H_{ND} = 30 nm nanodisks (Figures S26–S28). This confirms that the H_{ND} = 30 nm nanodisk height represents a practical optimum between fabrication yield, optical coupling, and photocatalytic performance.

The complex photocatalytic reaction kinetics require further consideration of the chemical interaction between the photocatalyst and the reaction sites. These could be assessed through computational methods, such as density functional theory (DFT) calculations on an atomistic scale [94]. These can provide theoretical insight into material-specific adsorption energies and reaction selectivity, which play crucial roles in determining the effectiveness of photocatalytic reactions. Nevertheless, our experiments quantify the performance of our plasmonically enhanced catalysts and show that both plasmonic interactions and adsorption properties must be considered, as reaction dynamics are primarily determined by adsorption, even though plasmonic interactions are clearly mediated by our metal nanostructures.

3 | Conclusion

We investigated plasmonic metamaterial photocatalyst sheets based on plasmonic nanodisks fabricated via scalable semiconductor device fabrication processes. The key processing step is

16136829, 0, Downloaded from https://onlinelibrary.wiley.com/doi/10.1002/smll.76358 by Universitatsbibliothek RWTH Aachen University, Wiley Online Library on [03/11/2026]. See the Terms and Conditions (https://onlinelibrary.wiley.com/terms-and-conditions) on Wiley Online Library for rules of use; OA articles are governed by the applicable Creative Commons License

NIL, which provides reliable, fast, and cost-efficient large-area patterning at the nanoscale. The resulting metamaterials comprise circular nanodisk arrays arranged in a square pattern with a period of 300 nm. We compared Ag, Au, Pt, and Pd as plasmonic nanodisks on a TiO_2 thin film layer. Our (5 × 5) cm^2 plasmonic metamaterial photocatalyst sheets show efficient IPA-assisted water splitting and CO_2 reduction together forming H_2 and CH_4 at rates of up to 4.37 μmol cm^{-2} h^{-1} and 0.42 μmol cm^{-2} h^{-1}, respectively. These high reaction rates were achieved using a custom-built reactor operating in the gaseous phase, with IPA as a hole scavenger and a 150 W HMI lamp as the visible broadband (UV–vis–NIR) light source. The highest CH_4 rates were achieved with Pd/TiO_2 samples, with an enhancement factor of 35.9 relative to Pd-TiO_2 combined photocatalysts. This high performance is mainly attributed to the periodic arrangement of the nanodisks, which combines plasmonic co-catalysts (Ag, Au, Pt, or Pd) with the photocatalytic thin-film material, anatase-phase TiO_2. The design of the metamaterial photocatalyst is flexible, as it can be modified by varying material choices or adjusting geometric parameters to develop an optimized photocatalyst sheet.

4 | Methods

4.1 | Metamaterial Photocatalyst Sheet Fabrication

First, 250 nm thin films of TiO_2 were deposited by magnetron sputtering on (5 × 5) cm^2-sized substrates as the photocatalysts. The substrates were either silicon (Si) or borosilicate glass. The TiO_2 films were subsequently annealed at 650 °C for 1 h to obtain the anatase crystal phase in the TiO_2 layer [74, 97]. Next, the PMMA and AMONIL resist layers were spin-coated, and arrays of 150 nm diameter holes with a period of 300 nm were formed via nanoimprint lithography (NIL) in the AMONIL with a master wafer fabricated with LIL (see below). Afterward, reactive ion etching (RIE) was used to dry-etch the residual AMONIL and the PMMA down to the TiO_2 layer. Then, 30 nm of the desired plasmonic metals were evaporated by electron beam evaporation on the photocatalyst. In the last step, the double-layer resist was lifted off [98]. The fabrication process of the photocatalyst sheet is outlined schematically in Figure S1.

4.2 | FDTD Simulations

The E-field enhancement and optical property simulations were computed with Ansys Lumerical software. Within the software, one period of the nanodisk array with a 300 nm period, 30 nm disk height, and 150 nm diameter was defined on top of a 250 nm TiO_2 layer. The broadband plane-wave light source in the software ranged from 200 to 1000 nm.

4.3 | Magnetron Sputtering

The TiO_2 thin-film layer was DC sputtered with a Creavac Creamet 500 S2 confocal magnetron sputtering system (Figure S1, Step 1). The gas flow was set to 80 sccm Ar and 6 sccm O_2. The substrate holder height was 100 cm, and the substrate rotation speed was 1 rpm. This process ensured a crystalline and rough TiO_2 layer, which is ideal for photocatalytic applications.

4.4 | Annealing

Since the TiO_2 layer crystallinity immediately after magnetron sputtering is amorphous, the sample requires an annealing step to form an anatase crystal phase (Figure S1, Step 1). The annealing process was conducted in a commercial rapid thermal annealing (RTA) furnace (AnnealSys Jipelec) for 1 h at 650°C.

4.5 | Laser Interference Lithography (LIL)

The 150-mm-sized master wafers for the NIL process were structured by laser interference lithography (LIL). The optical setup is custom-made and equipped with a 266 nm UV laser. The master structure was a hole pattern with a depth of 200 nm, a diameter of 150 nm, and a period of 300 nm.

4.6 | Nanoimprint Lithography (NIL)

The master structure fabricated from LIL was first duplicated with a polydimethylsiloxane (PDMS) stamp. Then, a double-layer resist of 100 nm PMMA and 100 nm AMONIL was spin-coated on the TiO_2 thin film (Figure S1, Step 3). PMMA was required for the later lift-off step, since it was difficult to strip off the AMONIL layer without damaging the underlying surface. The stamp was then attached to the photocatalyst in a SUSS MA8 mask aligner to perform the NIL process with a 320 nm UV lamp (Figure S1, Step 3). After the exposure time of 1 min, the stamp was released, and the stamp pattern was transferred onto the AMONIL layer.

4.7 | Reactive Ion Etching (RIE)

The dry-etching steps (Figure S1, Step 4) were conducted with an Oxford Instruments Plasmalab System 100. The AMONIL residual layer was removed via a CHF_3-based process, whereas a CF_4-based process was applied to etch PMMA.

4.8 | E-Beam Evaporation

All the metals (Figure S1, Step 5) were deposited with a thickness of 30 nm. Two commercial E-beam evaporation systems, Pfeiffer Classic 580 and Balzers PLS 500, were used because of their different material availability.

4.9 | Lift-Off Step

A lift-off process (Figure S1, Step 6) removed the PMMA-AMONIL double layer by soaking the photocatalyst in dimethylsulfoxide (DMSO) in an ultrasonic bath for 10 min. Afterward, the sample was cleaned with IPA and deionized (DI) water.

16136829, 0, Downloaded from https://onlinelibrary.wiley.com/doi/10.1002/smll.76358 by Universitatsbibliothek RWTH Aachen University, Wiley Online Library on [03/11/2026]. See the Terms and Conditions (https://onlinelibrary.wiley.com/terms-and-conditions) on Wiley Online Library for rules of use; OA articles are governed by the applicable Creative Commons License

4.10 | Atomic Force Microscopy (AFM)

Tapping mode AFM scans were performed with a Bruker Dimension Icon. Scan sizes of (3×3) μm^2 of the nanodisk metasurfaces were recorded at a scan rate of 0.5 Hz. The images were analyzed with the open-source software Gwyddion.

4.11 | Scanning Electron Microscopy (SEM)

Top-down and cross-sectional SEM images were taken with a Zeiss Supra 60VP. The images were taken with 50 000 × magnification, 4 keV electron high tension (EHT), and in a range of 5–8 mm working distance.

4.12 | UV–vis–NIR Spectrometry

Reflection (R) and transmission (T) measurements in the 200–1000 nm wavelength range were conducted with a PerkinElmer Lambda 1050+. The absorption (A) of the photocatalyst was obtained by calculating $A = 1 - R - T$. A full optical characterization is only possible on a glass substrate.

4.13 | Raman Spectroscopy

The Raman spectra were characterized with a Horiba Xplora within the range of 200–1000 cm^{-1} with a 532 nm green laser. The analysis was performed by fitting the Lorentzian curve at the Raman shift peaks.

Author Contributions

Benny Ku: investigation, writing – original draft, methodology, validation, formal analysis, data curation, visualization. **Lukas Feierabend**: investigation, methodology, writing – review and editing. **Chun-Wei Su**: writing – review and editing, investigation. **Chih-Chi Huang**: investigation, writing – review and editing. **Gonzalo Aguila Flores**: investigation, methodology, writing – review and editing. **Ulrich Plachetka**: conceptualization, methodology, validation, funding acquisition, writing – review and editing, project administration, resources, supervision. **Max C. Lemme**: supervision, resources, writing – review and editing, validation, conceptualization, funding acquisition.

Acknowledgements

The authors acknowledge Dr. Christine Hendriks for providing detailed structural and language feedback on the manuscript. The authors gratefully acknowledge the funding provided by the EFRE.NRW project Hypersol (EFRE-0801494), the EFRE.NRW project Roll2Sol (EFRE-20800213), and the Bundesministerium für Wirtschaft und Klimaschutz (BMWK) project COSMOS (49VF210041).

Open access funding enabled and organized by Projekt DEAL.

Conflicts of Interest

The authors declare no conflicts of interest.

Data Availability Statement

The data that support the findings of this study are available from the corresponding author upon reasonable request.

References

1. V. Smil, "Decarbonization Is Our Costliest Challenge: It Has No Clear Beginning or End, and it Affects Every Aspect of Life," *IEEE Spectrum* 59, no. 10 (2022): 22–23, https://doi.org/10.1109/mspec.2022.9915632.

2. M. Filonchyk, M. P. Peterson, L. Zhang, V. Hurynovich, and Y. He, "Greenhouse Gases Emissions and Global Climate Change: Examining the influence of CO_2, CH_4, and N_2O," *Science of the Total Environment* 935 (2024): 173359, https://doi.org/10.1016/j.scitotenv.2024.173359.

3. Z. Deng, B. Zhu, S. J. Davis, et al., "Global Carbon Emissions and Decarbonization in 2024," *Nature Reviews Earth & Environment* 6, no. 4 (2025): 231–233, https://doi.org/10.1038/s43017-025-00658-x.

4. G. Segev, J. Kibsgaard, C. Hahn, et al., "The 2022 Solar Fuels Roadmap," *Journal of Physics D: Applied Physics* 55, no. 32 (2022): 323003, https://doi.org/10.1088/1361-6463/ac6f97.

5. T. Hisatomi, T. Yamada, H. Nishiyama, T. Takata, and K. Domen, "Materials and Systems for Large-Scale Photocatalytic Water Splitting," *Nature Reviews Materials* 10, no. 10 (2025): 769–782, https://doi.org/10.1038/s41578-025-00823-0.

6. S. Anwar, Z. Aslam, U. Aslam, et al., "Advances and Challenges in Photocatalytic Water Splitting: Recent Developments and Trends," *Fuel* 404 (2026): 136280, https://doi.org/10.1016/j.fuel.2025.136280.

7. J. Kosco, F. Moruzzi, B. Willner, and I. McCulloch, "Photocatalysts Based on Organic Semiconductors With Tunable Energy Levels for Solar Fuel Applications," *Advanced Energy Materials* 10, no. 39 (2020): 2001935, https://doi.org/10.1002/aenm.202001935.

8. S. Chakraborty and S. C. Peter, "Solar-Fuel Production by Photodriven CO_2 Reduction: Facts, Challenges, and Recommendations," *ACS Energy Letters* 10, no. 5 (2025): 2359–2371, https://doi.org/10.1021/acsenergylett.5c00437.

9. A. Razzaq and S.-I. In, "TiO_2 Based Nanostructures for Photocatalytic CO_2 Conversion to Valuable Chemicals," *Micromachines* 10, no. 5 (2019): 326, https://doi.org/10.3390/mi10050326.

10. N. Shehzad, M. Tahir, K. Johari, T. Murugesan, and M. Hussain, "A Critical Review on TiO_2 Based Photocatalytic CO_2 Reduction System: Strategies to Improve Efficiency," *Journal of CO2 Utilization* 26 (2018): 98–122, https://doi.org/10.1016/j.jcou.2018.04.026.

11. W. Zhang, H. He, H. Li, et al., "Visible-Light Responsive TiO_2-Based Materials for Efficient Solar Energy Utilization," *Advanced Energy Materials* 11, no. 15 (2021): 2003303, https://doi.org/10.1002/aenm.202003303.

12. Y. Wei, L. Zou, H. Wang, Y. Wang, and Q. Xu, "Micro/Nano-Scaled Metal-Organic Frameworks and Their Derivatives for Energy Applications," *Advanced Energy Materials* 12, no. 4 (2022): 2003970, https://doi.org/10.1002/aenm.202003970.

13. X. Zou, Q. Shi, M. Cheng, et al., "Metal–Organic Framework-Based Materials for Photocatalytic Hydrogen Peroxide Production: Insights into Mechanism, Modification Strategies, and Environmental Applications," *Advanced Energy Materials* 15, no. 30 (2025): 2501424, https://doi.org/10.1002/aenm.202501424.

14. H. Hu, X. Li, K. Zhang, et al., "Dual Modification of Metal–Organic Frameworks for Exceptional High Piezo-Photocatalytic Hydrogen Production," *Advanced Materials* 37, no. 20 (2025): 2419023, https://doi.org/10.1002/adma.202419023.

15. X. Zhang, Y. L. Chen, R.-S. Liu, and D. P. Tsai, "Plasmonic Photocatalysis," *Reports on Progress in Physics* 76, no. 4 (2013): 046401, https://doi.org/10.1088/0034-4885/76/4/046401.

16. S. Li, P. Miao, Y. Zhang, et al., "Recent Advances in Plasmonic Nanostructures for Enhanced Photocatalysis and Electrocatalysis," *Advanced Materials* 33, no. 6 (2021): 2000086, https://doi.org/10.1002/adma.202000086.

17. L. Chaabane and I. Trendafilova, "Plasmonic Nanostructures for Enhanced Photocatalytic Overall Water Splitting," *Iscience* 28, no. 7 (2025): 112799, https://doi.org/10.1016/j.isci.2025.112799.

16136829, 0, Downloaded from https://onlinelibrary.wiley.com/doi/10.1002/smll.76358 by Universitatsbibliothek RWTH Aachen University, Wiley Online Library on [03/11/2026]. See the Terms and Conditions (https://onlinelibrary.wiley.com/terms-and-conditions) on Wiley Online Library for rules of use; OA articles are governed by the applicable Creative Commons License

18. H. Huang, B. Pradhan, J. Hofkens, M. B. J. Roeffaers, and J. A. Steele, "Solar-Driven Metal Halide Perovskite Photocatalysis: Design, Stability, and Performance," *ACS Energy Letters* 5, no. 4 (2020): 1107–1123, https://doi.org/10.1021/acsenergylett.0c00058.

19. A. Baray-Calderón, J. L. Aleman-Ramirez, E. B. Díaz-Cruz, et al., "Recent Advances in Perovskite-Based Heterojunction Photocatalysts: Synthesis, Properties, and Applications," *Korean Journal of Chemical Engineering* 42, no. 4 (2025): 803–826, https://doi.org/10.1007/s11814-025-00416-1.

20. İ. Kalkan and A. Koca, "Recent Advances in Perovskites for Electrocatalytic and Photocatalytic Water Splitting Processes: Materials, Characterizations, Synthesis and Applications," *Sustainable Energy & Fuels* 9, no. 22 (2025): 6050–6096, https://doi.org/10.1039/D5SE01051A.

21. J. Low, J. Yu, and W. Ho, "Graphene-Based Photocatalysts for CO_2 Reduction to Solar Fuel," *The Journal of Physical Chemistry Letters* 6, no. 21 (2015): 4244–4251, https://doi.org/10.1021/acs.jpclett.5b01610.

22. Z. Li, X. Meng, and Z. Zhang, "Recent Development on MoS_2-Based Photocatalysis: A Review," *Journal of Photochemistry and Photobiology C: Photochemistry Reviews* 35 (2018): 39–55, https://doi.org/10.1016/j.jphotochemrev.2017.12.002.

23. X. Zhang, A. Chen, L. Chen, and Z. Zhou, "2D Materials Bridging Experiments and Computations for Electro/Photocatalysis," *Advanced Energy Materials* 12, no. 4 (2022): 2003841, https://doi.org/10.1002/aenm.202003841.

24. S. Ezendam, M. Herran, L. Nan, et al., "Hybrid Plasmonic Nanomaterials for Hydrogen Generation and Carbon Dioxide Reduction," *ACS Energy Letters* 7, no. 2 (2022): 778–815, https://doi.org/10.1021/acsenergylett.1c02241.

25. J. Schneidewind, "How Much Technological Progress Is Needed to Make Solar Hydrogen Cost-Competitive?," *Advanced Energy Materials* 12, no. 18 (2022): 2200342, https://doi.org/10.1002/aenm.202200342.

26. S. Nandy, T. Hisatomi, T. Takata, T. Setoyama, and K. Domen, "Recent Advances in Photocatalyst Sheet Development and Challenges for Cost-Effective Solar Hydrogen Production," *Journal of Materials Chemistry A* 11, no. 38 (2023): 20470–20479, https://doi.org/10.1039/D3TA04353C.

27. Y. Goto, T. Hisatomi, Q. Wang, et al., "A Particulate Photocatalyst Water-Splitting Panel for Large-Scale Solar Hydrogen Generation," *Joule* 2, no. 3 (2018): 509–520, https://doi.org/10.1016/j.joule.2017.12.009.

28. Q. Wang, T. Hisatomi, Q. Jia, et al., "Scalable Water Splitting on Particulate Photocatalyst Sheets With a Solar-to-Hydrogen Energy Conversion Efficiency Exceeding 1%," *Nature Materials* 15, no. 6 (2016): 611–615, https://doi.org/10.1038/nmat4589.

29. M. R. Alfaro Cruz, A. Saldaña-Ramírez, I. Juárez-Ramírez, and L. M. Torres-Martínez, "Enhanced Photocatalytic Hydrogen Production via Optimised ZnO–SnO_2 Thin Films: The Role of Sputtering Conditions," *Materials Research Innovations* 30, no. 1 (2026): 18–33, https://doi.org/10.1080/14328917.2025.2521619.

30. K. Yao and Y. Liu, "Plasmonic Metamaterials," *Nanotechnology Reviews* 3, no. 2 (2014): 177–210, https://doi.org/10.1515/ntrev-2012-0071.

31. F. Monticone and A. Alù, "Metamaterial, Plasmonic and Nanophotonic Devices," *Reports on Progress in Physics* 80, no. 3 (2017): 036401, https://doi.org/10.1088/1361-6633/aa518f.

32. J. Y. Y. Loh, "Could Metamaterials be the Next Frontier of Catalysis?," *Small* 21, no. 4 (2025): 2405140, https://doi.org/10.1002/smll.202405140.

33. M. Torras, P. Molet, L. Soler, J. Llorca, A. Roig, and A. Mihi, "Au/TiO_2 2D-Photonic Crystals as UV–Visible Photocatalysts for H_2 Production," *Advanced Energy Materials* 12, no. 6 (2022): 2103733, https://doi.org/10.1002/aenm.202103733.

34. R. Xu, L. Wen, Z. Wang, et al., "Three-Dimensional Plasmonic Nanostructure Design for Boosting Photoelectrochemical Activity," *ACS Nano* 11, no. 7 (2017): 7382–7389, https://doi.org/10.1021/acsnano.7b03633.

35. D. Daskalova, G. Aguila Flores, and U. Plachetka, "Combined Structural and Plasmonic Enhancement of Nanometer-Thin Film Photocatalysis for Solar-Driven Wastewater Treatment," *ACS Applied Nano Materials* 6, no. 16 (2023): 15204–15212, https://doi.org/10.1021/acsanm.3c02867.

36. J. Y. Y. Loh, R. Chhorn, G. Sharma, et al., "Superblackbody Metasurface Activates CO_2 Vibrational Mode for Enhanced Selectivity in CO_2 Reduction," *ACS Nano* 20, no. 21 (2026): 15372–15383, https://doi.org/10.1021/acsnano.6c03111.

37. Y.-N. Jing, X.-L. Yin, and L. Li, "Modification Strategies of TiO_2-Based Nanocatalysts for CO_2 Reduction Through Photocatalysis: A Mini Review," *Applied Catalysis A: General* 691 (2025): 120054, https://doi.org/10.1016/j.apcata.2024.120054.

38. L. Yuan, C. Zhang, X. Zhang, et al., "Photocatalytic Hydrogenation of Graphene Using Pd Nanocones," *Nano Letters* 19, no. 7 (2019): 4413–4419, https://doi.org/10.1021/acs.nanolett.9b01121.

39. Z. Li and X. Meng, "Recent Development on Palladium Enhanced Photocatalytic Activity: A Review," *Journal of Alloys and Compounds* 830 (2020): 154669, https://doi.org/10.1016/j.jallcom.2020.154669.

40. L. Mascaretti and A. Naldoni, "Hot Electron and Thermal Effects in Plasmonic Photocatalysis," *Journal of Applied Physics* 128, no. 4 (2020): 041101, https://doi.org/10.1063/5.0013945.

41. H. Huang, R. Shi, Z. Li, J. Zhao, C. Su, and T. Zhang, "Triphase Photocatalytic CO_2 Reduction over Silver-Decorated Titanium Oxide at a Gas–Water Boundary," *Angewandte Chemie International Edition* 61, no. 17 (2022): 202200802, https://doi.org/10.1002/anie.202200802.

42. D. Hong, L.-M. Lyu, K. Koga, et al., "Plasmonic Ag@TiO_2 Core–Shell Nanoparticles for Enhanced CO_2 Photoconversion to CH_4," *ACS Sustainable Chemistry & Engineering* 7, no. 23 (2019): 18955–18964, https://doi.org/10.1021/acssuschemeng.9b04345.

43. S. Feng, M. Wang, Y. Zhou, Y. Shimoyama, and Y. Kon, "Double-Shelled Plasmonic Ag-TiO_2 Hollow Spheres Toward Visible Light-Active Photocatalytic Conversion of CO_2 Into Solar Fuel," *APL Materials* 3, no. 10 (2015): 104416, https://doi.org/10.1063/1.4930043.

44. R. Wang, J. Shen, K. Sun, H. Tang, and Q. Liu, "Enhancement in Photocatalytic Activity of CO_2 Reduction to CH_4 by 0D/2D Au/TiO_2 Plasmon Heterojunction," *Applied Surface Science* 493 (2019): 1142–1149, https://doi.org/10.1016/j.apsusc.2019.07.121.

45. M. Tahir, B. Tahir, and N. A. S. Amin, "Gold-Nanoparticle-Modified TiO_2 Nanowires for Plasmon-Enhanced Photocatalytic CO_2 Reduction With H_2 Under Visible Light Irradiation," *Applied Surface Science* 356 (2015): 1289–1299, https://doi.org/10.1016/j.apsusc.2015.08.231.

46. W. Hou, W. H. Hung, P. Pavaskar, A. Goeppert, M. Aykol, and S. B. Cronin, "Photocatalytic Conversion of CO_2 to Hydrocarbon Fuels via Plasmon-Enhanced Absorption and Metallic Interband Transitions," *ACS Catalysis* 1, no. 8 (2011): 929–936, https://doi.org/10.1021/cs2001434.

47. A. Pougin, G. Dodekatos, M. Dilla, H. Tüysüz, and J. Strunk, "Au@TiO_2 Core-Shell Composites for the Photocatalytic Reduction of CO_2," *Chemistry – A European Journal* 24, no. 47 (2018): 12416–12425, https://doi.org/10.1002/chem.201801796.

48. A. Durga Devi, S. Pushpavanam, N. Singh, J. Verma, M. P. Kaur, and S. C. Roy, "Enhanced Methane Yield by Photoreduction of CO_2 at Moderate Temperature and Pressure Using Pt Coated, Graphene Oxide Wrapped TiO_2 Nanotubes," *Results in Engineering* 14 (2022): 100441, https://doi.org/10.1016/j.rineng.2022.100441.

49. W.-N. Wang, W.-J. An, B. Ramalingam, et al., "Size and Structure Matter: Enhanced CO_2 Photoreduction Efficiency by Size-Resolved Ultrafine Pt Nanoparticles on TiO_2 Single Crystals," *Journal of the American Chemical Society* 134, no. 27 (2012): 11276–11281, https://doi.org/10.1021/ja304075b.

50. S. Sorcar, Y. Hwang, C. A. Grimes, and S.-I. In, "Highly Enhanced and Stable Activity of Defect-Induced Titania Nanoparticles for Solar Light-Driven CO_2 Reduction Into CH_4," *Materials Today* 20, no. 9 (2017): 507–515, https://doi.org/10.1016/j.mattod.2017.09.005.

16136829, 0, Downloaded from https://onlinelibrary.wiley.com/doi/10.1002/smll.76358 by Universitatsbibliothek RWTH Aachen University, Wiley Online Library on [03/11/2026]. See the Terms and Conditions (https://onlinelibrary.wiley.com/terms-and-conditions) on Wiley Online Library for rules of use; OA articles are governed by the applicable Creative Commons License

51. M. Moradi, F. Khorasheh, and A. Larimi, "Pt Nanoparticles Decorated Bi-Doped TiO_2 as an Efficient Photocatalyst for CO_2 Photo-Reduction Into CH_4," *Solar Energy* 211 (2020): 100–110, https://doi.org/10.1016/j.solener.2020.09.054.

52. S. Xie, Y. Wang, Q. Zhang, W. Deng, and Y. Wang, "MgO- and Pt-Promoted TiO_2 as an Efficient Photocatalyst for the Preferential Reduction of Carbon Dioxide in the Presence of Water," *ACS Catalysis* 4, no. 10 (2014): 3644–3653, https://doi.org/10.1021/cs500648p.

53. Y. Ma, X. Yi, and S. Wang, "Selective Photocatalytic CO_2 Reduction in Aerobic Environment by Microporous Pd-Porphyrin-Based Polymers Coated Hollow TiO_2," *Nature Communications* 13, no. 1 (2022): 1400, https://doi.org/10.1038/s41467-022-29102-0.

54. T. Yui, A. Kan, C. Saitoh, K. Koike, T. Ibusuki, and O. Ishitani, "Photochemical Reduction of CO_2 Using TiO_2 : Effects of Organic Adsorbates on TiO_2 and Deposition of Pd Onto TiO_2," *ACS Applied Materials & Interfaces* 3, no. 7 (2011): 2594–2600, https://doi.org/10.1021/am200425y.

55. K.-Y. Su, C.-Y. Chen, and R.-J. Wu, "Preparation of Pd/TiO_2 Nanowires for the Photoreduction of CO_2 Into Renewable Hydrocarbon Fuels," *Journal of the Taiwan Institute of Chemical Engineers* 96 (2019): 409–418, https://doi.org/10.1016/j.jtice.2018.12.010.

56. J. W. Sadowski, J. Lekkala, and I. Vikholm, "Biosensors Based on Surface Plasmons Excited in Non-Noble Metals," *Biosensors and Bioelectronics* 6, no. 5 (1991): 439–444, https://doi.org/10.1016/0956-5663(91)87009-Z.

57. G. S. Karlberg, "Adsorption Trends for Water, Hydroxyl, Oxygen, and Hydrogen on Transition-Metal and Platinum-Skin Surfaces," *Physical Review B* 74, no. 15 (2006): 153414, https://doi.org/10.1103/PhysRevB.74.153414.

58. J. K. Nørskov, F. Abild-Pedersen, F. Studt, and T. Bligaard, "Density Functional Theory in Surface Chemistry and Catalysis," *Proceedings of the National Academy of Sciences* 108, no. 3 (2011): 937–943, https://doi.org/10.1073/pnas.1006652108.

59. L. Wen, R. Xu, C. Cui, et al., "Template-Guided Programmable Janus Heteronanostructure Arrays for Efficient Plasmonic Photocatalysis," *Nano Letters* 18, no. 8 (2018): 4914–4921, https://doi.org/10.1021/acs.nanolett.8b01675.

60. P. Xie, Z. Chen, J. Xu, et al., "Artificial Ceramic Diatoms With Multiscale Photonic Architectures via Nanoimprint Lithography for CO_2 Photoreduction," *Journal of the American Ceramic Society* 102, no. 8 (2019): 4678–4687, https://doi.org/10.1111/jace.16334.

61. T. Ifuku, M. Yonekawa, and K. Nakagawa, "Nanoimprint Lithography Performance Advances for New Application Spaces," in *Novel Patterning Technologies*, eds. J. A. Liddle, R. Ruiz (SPIE, 2024), 10, https://doi.org/10.1117/12.3012070.

62. I. S. Garcia, A. Retolaza, C. Ferreira, et al., "Nanoimprint Lithography for Grayscale Pattern Replication of MEMS Mirrors in a 200 mm Wafer," *Journal of Manufacturing Processes* 116 (2024): 202–209, https://doi.org/10.1016/j.jmapro.2024.02.039.

63. J. Fujisawa, T. Eda, and M. Hanaya, "Comparative Study of Conduction-Band and Valence-Band Edges of TiO_2, $SrTiO_3$, and $BaTiO_3$ by Ionization Potential Measurements," *Chemical Physics Letters* 685 (2017): 23–26, https://doi.org/10.1016/j.cplett.2017.07.031.

64. D. O. Scanlon, C. W. Dunnill, J. Buckeridge, et al., "Band Alignment of Rutile and Anatase TiO_2," *Nature Materials* 12, no. 9 (2013): 798–801, https://doi.org/10.1038/nmat3697.

65. V. Mansfeldova, M. Zlamalova, H. Tarabkova, et al., "Work Function of TiO_2 (Anatase, Rutile, and Brookite) Single Crystals: Effects of the Environment," *The Journal of Physical Chemistry C* 125, no. 3 (2021): 1902–1912, https://doi.org/10.1021/acs.jpcc.0c10519.

66. P. T. Moseley, "Progress in the Development of Semiconducting Metal Oxide Gas Sensors: A Review," *Measurement Science and Technology* 28, no. 8 (2017): 082001, https://doi.org/10.1088/1361-6501/aa7443.

67. M. Ahlawat, D. Mittal, and V. G. Rao, "Plasmon-Induced Hot-Hole Generation and Extraction at Nano-Heterointerfaces for Photocatalysis," *Communications Materials* 2, no. 1 (2021): 114, https://doi.org/10.1038/s43246-021-00220-4.

68. A. Ziashahabi, M. Prato, Z. Dang, R. Poursalehi, and N. Naseri, "The Effect of Silver Oxidation on the Photocatalytic Activity of Ag/ZnO Hybrid Plasmonic/Metal-Oxide Nanostructures Under Visible Light and in the Dark," *Scientific Reports* 9, no. 1 (2019): 11839, https://doi.org/10.1038/s41598-019-48075-7.

69. M. Hassani-Gangaraj, D. Veysset, K. A. Nelson, et al., "Impact-Bonding With Aluminum, Silver, and Gold Microparticles: Toward Understanding the Role of Native Oxide Layer," *Applied Surface Science* 476 (2019): 528–532, https://doi.org/10.1016/j.apsusc.2019.01.111.

70. W. Jiang, X. Wang, Z. Wu, et al., "Silver Oxide as Superb and Stable Photocatalyst under Visible and Near-Infrared Light Irradiation and Its Photocatalytic Mechanism," *Industrial & Engineering Chemistry Research* 54, no. 3 (2015): 832–841, https://doi.org/10.1021/ie503241k.

71. Y. Wang and C. Wöll, "IR Spectroscopic Investigations of Chemical and Photochemical Reactions on Metal Oxides: Bridging the Materials Gap," *Chemical Society Reviews* 46, no. 7 (2017): 1875–1932, https://doi.org/10.1039/C6CS00914J.

72. H. Issa Hamoud, L. Wolski, I. Pankin, M. A. Bañares, M. Daturi, and M. El-Roz, "In situ and Operando Spectroscopies in Photocatalysis: Powerful Techniques for a Better Understanding of the Performance and the Reaction Mechanism," *Topics in Current Chemistry* 380, no. 5 (2022): 37, https://doi.org/10.1007/s41061-022-00387-5.

73. S. M. Kim, C. Lee, K. C. Goddeti, and J. Y. Park, "Hot Plasmonic Electron-Driven Catalytic Reactions on Patterned Metal–Insulator–Metal Nanostructures," *Nanoscale* 9, no. 32 (2017): 11667–11677, https://doi.org/10.1039/C7NR02805A.

74. T. Luttrell, S. Halpegamage, J. Tao, A. Kramer, E. Sutter, and M. Batzill, "Why Is Anatase a Better Photocatalyst Than Rutile? – Model Studies on Epitaxial Tio_2 Films," *Scientific Reports* 4, no. 1 (2015): 4043, https://doi.org/10.1038/srep04043.

75. C. Casado, J. Marugán, R. Timmers, M. Muñoz, and R. Grieken, "Comprehensive Multiphysics Modeling of Photocatalytic Processes by Computational Fluid Dynamics Based on Intrinsic Kinetic Parameters Determined in a Differential Photoreactor," *Chemical Engineering Journal* 310 (2017): 368–380, https://doi.org/10.1016/j.cej.2016.07.081.

76. T. A. Kandiel, L. Robben, A. Alkaima, and D. Bahnemann, "Brookite Versus Anatase TiO_2 Photocatalysts: Phase Transformations and Photocatalytic Activities," *Photochemical & Photobiological Sciences* 12, no. 4 (2013): 602–609, https://doi.org/10.1039/c2pp25217a.

77. H. Li, T. Wang, S. Liu, et al., "Controllable Distribution of Oxygen Vacancies in Grain Boundaries of p-Si/TiO_2 Heterojunction Photocathodes for Solar Water Splitting," *Angewandte Chemie International Edition* 60, no. 8 (2021): 4034–4037, https://doi.org/10.1002/anie.202014538.

78. N. S. Allen, N. Mahdjoub, V. Vishnyakov, et al., "The Effect of Crystalline Phase (Anatase, Brookite and Rutile) and Size on the Photocatalytic Activity of Calcined Polymorphic Titanium Dioxide (TiO_2)," *Polymer Degradation and Stability* 150 (2018): 31–36, https://doi.org/10.1016/j.polymdegradstab.2018.02.008.

79. I. L. Rasskazov, N. Sonwalkar, and P. S. Carney, "Light Scattering by Plasmonic Disks and Holes Arrays: Different or the Same?," *Journal of Physics D: Applied Physics* 55, no. 45 (2022): 455104, https://doi.org/10.1088/1361-6463/ac8ffc.

80. S. Hamdad, A. T. Diallo, M. Chakaroun, and A. Boudrioua, "The Role of Rayleigh Anomalies in the Coupling Process of Plasmonic Gratings and the Control of the Emission Properties of Organic Molecules," *Scientific Reports* 12, no. 1 (2022): 3218, https://doi.org/10.1038/s41598-022-07216-1.

81. F. Costantino and P. V. Kamat, "Do Sacrificial Donors Donate H2 in Photocatalysis?," *ACS Energy Letters* 7, no. 1 (2022): 242–246, https://doi.org/10.1021/acsenergylett.1c02487.

16136829, 0, Downloaded from https://onlinelibrary.wiley.com/doi/10.1002/smll.76358 by Universitatsbibliothek RWTH Aachen University, Wiley Online Library on [03/11/2026]. See the Terms and Conditions (https://onlinelibrary.wiley.com/terms-and-conditions) on Wiley Online Library for rules of use; OA articles are governed by the applicable Creative Commons License

82. H. Park, H.-H. Ou, U. Kang, J. Choi, and M. R. Hoffmann, "Photocatalytic Conversion of Carbon Dioxide to Methane on TiO_2/CdS in Aqueous Isopropanol Solution," *Catalysis Today* 266 (2016): 153–159, https://doi.org/10.1016/j.cattod.2015.09.017.

83. A. Augustin, P. Ganguly, S. Shenoy, et al., "Impact of Hole Scavengers on Efficient Photocatalytic Hydrogen Production," *Advanced Sustainable Systems* 8, no. 12 (2024): 2400321, https://doi.org/10.1002/adsu.202400321.

84. S. Yu and P. K. Jain, "Selective Branching of Plasmonic Photosynthesis Into Hydrocarbon Production and Hydrogen Generation," *ACS Energy Letters* 4, no. 9 (2019): 2295–2300, https://doi.org/10.1021/acsenergylett.9b01688.

85. J. Ran, M. Jaroniec, and S. Qiao, "Cocatalysts in Semiconductor-Based Photocatalytic CO_2 Reduction: Achievements, Challenges, and Opportunities," *Advanced Materials* 30, no. 7 (2018): 1704649, https://doi.org/10.1002/adma.201704649.

86. A. H. Assi, "Engineering Education and Research Using MATLAB," (IntechOpen, 2011), https://doi.org/10.5772/1532.

87. Y. Jiang, H. Chen, J. Li, et al., "Z-Scheme 2D/2D Heterojunction of $CsPbBr_3$/Bi_2WO_6 for Improved Photocatalytic CO_2 Reduction," *Advanced Functional Materials* 30, no. 50 (2020): 2004293, https://doi.org/10.1002/adfm.202004293.

88. Y. Y. Maruo, T. Yamada, and M. Tsuda, "Reactivity of CO_2 and H_2O on TiO_2 Catalysts Studied by Gas Phase FT-IR Method and Deactivation Mechanism," *Journal of Physics: Conference Series* 379 (2012): 012036, https://doi.org/10.1088/1742-6596/379/1/012036.

89. J. H. Bitter, K. Seshan, and J. A. Lercher, "Deactivation and Coke Accumulation During CO_2/CH_4 Reforming Over Pt Catalysts," *Journal of Catalysis* 183, no. 2 (1999): 336–343, https://doi.org/10.1006/jcat.1999.2402.

90. Y. Yang, Y. Ling, G. Wang, et al., "Photohole Induced Corrosion of Titanium Dioxide: Mechanism and Solutions," *Nano Letters* 15, no. 10 (2015): 7051–7057, https://doi.org/10.1021/acs.nanolett.5b03114.

91. Y. Li, Z. Zeng, Y. Zhang, et al., "Deactivation and Stabilization Mechanism of Photothermal CO_2 Hydrogenation Over Black TiO_2," *ACS Sustainable Chemistry & Engineering* 10, no. 19 (2022): 6382–6388, https://doi.org/10.1021/acssuschemeng.2c01081.

92. E. Pomerantseva, C. Resini, K. Kovnir, and Y. V. Kolen'ko, "Emerging Nanostructured Electrode Materials for Water Electrolysis and Rechargeable Beyond Li-Ion Batteries," *Advances in Physics: X* 2, no. 2 (2017): 211–253, https://doi.org/10.1080/23746149.2016.1273796.

93. G. N. Derry, M. E. Kern, and E. H. Worth, "Recommended Values of Clean Metal Surface Work Functions," *Journal of Vacuum Science & Technology A: Vacuum, Surfaces, and Films* 33, no. 6 (2015): 060801, https://doi.org/10.1116/1.4934685.

94. Ž. Kovačič, B. Likozar, and M. Huš, "Photocatalytic CO_2 Reduction: A Review of Ab Initio Mechanism, Kinetics, and Multiscale Modeling Simulations," *ACS Catalysis* 10, no. 24 (2020): 14984–15007, https://doi.org/10.1021/acscatal.0c02557.

95. S. N. Habisreutinger, L. Schmidt-Mende, and J. K. Stolarczyk, "Photocatalytic Reduction of CO_2 on TiO_2 and Other Semiconductors," *Angewandte Chemie International Edition* 52, no. 29 (2013): 7372–7408, https://doi.org/10.1002/anie.201207199.

96. Z. Chai, "Light-Driven Alcohol Splitting by Heterogeneous Photocatalysis: Recent Advances, Mechanism and Prospects," *Chemistry – An Asian Journal* 16, no. 5 (2021): 460–473, https://doi.org/10.1002/asia.202001312.

97. A. Vahl, S. Veziroglu, B. Henkel, et al., "Pathways to Tailor Photocatalytic Performance of TiO_2 Thin Films Deposited by Reactive Magnetron Sputtering," *Materials* 12, no. 17 (2019): 2840, https://doi.org/10.3390/ma12172840.

98. J. Barnett, U. Plachetka, C. Nowak, and H. Wackerbarth, "Highly Periodic Au Nano-Disc Arrays for Plasmon-Resonant SERS Structures on Fused Silica Using UV-NIL Based Double-Layer Lift-Off Process," *Microelectronic Engineering* 172 (2017): 45–48, https://doi.org/10.1016/j.mee.2017.02.02.

Supporting Information

Additional supporting information can be found online in the Supporting Information section.

Supporting File: smll76358-sup-0001-SuppMat.docx.

16136829, 0, Downloaded from https://onlinelibrary.wiley.com/doi/10.1002/smll.76358 by Universitatsbibliothek RWTH Aachen University, Wiley Online Library on [03/11/2026]. See the Terms and Conditions (https://onlinelibrary.wiley.com/terms-and-conditions) on Wiley Online Library for rules of use; OA articles are governed by the applicable Creative Commons License